ADVANCED PHYSICS RESEARCH Open Access
www.advphysicsres.com

Enhancing Signal Purity in Josephson Structure Measurements

*Ivan A. Nazhestkin, Georgy I. Gubochkin, Jonathan Shvartzberg, Sai-Prasad M. Rajam, Sergei V. Egorov, Vladimir L. Gurtovoi, Valery V. Ryazanov, Vasily S. Stolyarov, and Dmitry S. Yakovlev**

Abstract: Superconducting Josephson structures play a significant role in quantum-state engineering. Achieving high-fidelity quantum state measurements in superconducting Josephson structures requires ultra-low noise environments and robust signal purification techniques. Here, the advanced low-noise signal measurement system designed for dilution refrigerators is presented, integrating multi-stage cryogenic filtering and electromagnetic shielding strategies to suppress noise sources across a broad frequency spectrum. The effectiveness of low-pass RC filters is demonstrated, silver-epoxy microwave absorbers, and optimized ground isolation to achieve an unprecedented noise reduction, enabling sub-nanoampere switching current distribution measurements superior to commerical systems at mK temperatures. The system is optimized for precision studies of superconductor-insulator-superconductor, superconductor-ferromagnet-superconductor, and superconductor-normal metal-superconductor Josephson junctions with low critical currents. This approach establishes a reliable framework for next-generation quantum electronic experiments, ensuring that observed switching phenomena are governed by intrinsic device physics rather than environmental perturbations.

1. Introduction

Quantum-state engineering–active control over the coherent dynamics of quantum systems–has emerged as a cornerstone of modern physics.[1] Superconducting Josephson structures play a central role in this field, enabling precise manipulation of quantum states. However, achieving high-fidelity measurements necessitates an ultra-low-noise environment at millikelvin temperatures with minimal thermal fluctuations, electromagnetic interference (EMI), and residual radio-frequency (RF) signals. Such noise sources result in an increase in the effective electron temperature. This work explores filtering strategies designed to suppress noise and preserve signal integrity.

Signal purity in Josephson junction measurements requires aggressive filtering across various frequencies. Several filtering techniques have been

I. A. Nazhestkin, V. V. Ryazanov, V. S. Stolyarov
Moscow Institute of Physics and Technology
9 Institutskiy per., Dolgoprudny 141700, Russia

I. A. Nazhestkin, G. I. Gubochkin, S.-P. M. Rajam, V. V. Ryazanov
Russian Quantum Center
Skolkovo, Moscow Region 143025, Russia

G. I. Gubochkin
Faculty of Physics
Lomonosov Moscow State University
Moscow 119991, Russia

J. Shvartzberg
Institute of Superconductivity and Institute of Nanotechnology
Department of Physics
Bar-Ilan University
Ramat-Gan 5290002, Israel

S. V. Egorov
Laboratory of Superconductivity
Institute of Solid State Physics
142432 Chernogolovka, Russia

V. L. Gurtovoi
Institute of Microelectronics Technology and High Purity Materials
Russian Academy of Sciences
Chernogolovka 142432, Russia

D. S. Yakovlev
Laboratoire de Physique et d'étude des Matériaux, ESPCI Paris, CNRS
PSL University
Paris 75005, France
E-mail: dimitry.yakovlev@espci.fr

The ORCID identification number(s) for the author(s) of this article can be found under https://doi.org/10.1002/apxr.202500032

DOI: 10.1002/apxr.202500032

implemented since the 1980s. Traditional RC filters implemented on-chip[2–4] and in coaxial cables[5–7] are useful for attenuation of frequencies up to 10 MHz, beyond which π filters are needed.[8] Microwave frequencies greater than 100 MHz are best absorbed by transmission line filters[9–11] and metal powders whose large surface areas cause skin effect damping to strongly attenuate external fields.[12–18] Printed circuit board (PCB) based filters with metal powder enclosures,[8] distributed damping filters as thin films in a flip-chip[19] and carbon nanotube-based filters[20] have also been demonstrated. A very cost-effective filter design is the twisted pair filter enclosed by copper tape.[21,22] This "copper tapeworm" contains lesser quantity of metal to be cooled than metal powder filters. All filters heat up due to dissipation and inductive heating. Therefore, many of them use thermal epoxies and are thermally anchored to various stages of cryostats. Likewise, other components such as wires and sample holders are also thermally anchored to cryostat stages[23] because at ultra-low temperatures, the electron-phonon coupling drastically decreases and electron cooling happens largely via electrical contacts.[24] Modern filter implementations require cascades of low-pass filters at different temperature stages to eliminate external RF noise and ensure the device is at thermal equilibrium with the cryostat.[25–29] For example, a typical wiring chain may include a π-type feed through filter at room temperature (cutoff in the MHz range), followed by cryogenic low-pass filters at intermediate stages (e.g., an RC filter in the temperature range of 1–4K), and high-attenuation filters at the mixing chamber (10 mK stage) such as copper-powder or silver-epoxy filters.[26,30] At room temperature, *pi* filters (often realized as feed through capacitors) suppress radio-frequency interference above ∼10 MHz, while the cryogenic powder and epoxy filters provide >50–100 dB attenuation at GHz frequencies.[30] Notably, silver-epoxy-made microwave filters can achieve over 100 dB attenuation for $f > 150$ MHz (and even above 30 MHz when as built-in capacitors).[16] Such filters absorb high-frequency noise and protect the signal lines, preventing room-temperature black-body radiation from reaching the sample. Moreover, to ensure that the sample's "electronic temperature" remains equal to the refrigerator's base temperature, rigorous filtering of RF radiation is crucial.[25] Experiments have shown that with proper filtering (cutoffs of order kHz at cryogenic stages), the Josephson device avoids excess noise-induced switching and remains in equilibrium with the refrigerator. In practice, each filter stage is chosen to target a specific band of unwanted noise range: RC filters for low-frequency interference (e.g., 1/f or mains pickup), while broadband lossy-line filters (Thermocoax[5,31–33] or resistive twisted pairs embedded in metal powder) for high-frequency microwave spikes. These multi-stage filtering networks preserve signal integrity and yield ultra-sharp switching characteristics by attenuating noise from direct current (DC) up to the GHz range. Indeed, without such measures, environmental RF noise from radio stations, mobile phones, and ambient black-body radiation can propagate through the measurement cables and alter the results by spuriously broadening the observed switching current distribution.[26] However, with all three filter stages connected to the system, attenuation of 90 dB above ∼40 MHz (and $\gtrsim$ 110 dB beyond a few GHz) can be achieved,[26] effectively pushing residual noise to negligible levels and ensuring that the measured critical-switching events reflect the intrinsic junction properties rather than external perturbations.

In addition to dedicated filters, careful experimental design minimizes EMI and thermal noise in Josephson device measurements.[34,35] A common practice is to enclose the sample and sensitive wiring in a RF tight environment. For example, the sample chip is often mounted in a closed copper Faraday cage or an RF-tight copper can at the cryostat base temperature.[36–38] This shield blocks external electromagnetic radiation and prevents stray fields from coupling with the device.[39,40] All signal lines entering the enclosure are filtered and made of coaxial or twisted-pair wiring to reject inductive pickup.[41,42] Using twisted pair or superconducting coax leads (enclosed in a braided shield) significantly reduces the cross section and thus coupling of ambient alternating current (AC) fields. Additionally, sensor wires (for thermometers, heaters, etc.) are routed separately from high-frequency signal lines to avoid cross-talk.[43–46] To eliminate ground loops and external EMI, the entire measurement electronics are often placed in a single grounding scheme (e.g., a shielded room or enclosure) with the cryostat. Instrumentation may be battery-powered or use isolation transformers to decouple from noisy mains ground.[47] Crucially, the analog bias circuitry can be electrically isolated from any digital control circuitry by using optical fiber links or opto-couplers inside or outside the cryostat, as demonstrated in high-precision switching experiments.[12,48] By converting trigger signals to optical pulses and back, one prevents digital switching noise from propagating into the analog measurement loop. Thermal noise is mitigated by proper thermal anchoring and attenuation of the leads.[49] Each measurement line is anchored at multiple temperature stages using braid thermal ties or embedding the line in high-heat-capacity copper stages, so that by the time it reaches the mixing chamber the electrons in the lead are cooled to base temperature.[50,51] In practice, 20dB cryogenic attenuators (50Ω terminators) are often installed at the 4K and base stages; these not only attenuate incoming noise but also re-emit thermal noise only from the stage at which they are mounted (ensuring the noise spectral density corresponds to a few Kelvin rather than 300K). In combination with lossy filters (e.g., a resistive coax line acting as a distributed RC network), this prevents higher-temperature Johnson noise from reaching the sample. The result is that the dominant noise near the device is set by the coldest temperature stage, dramatically reducing thermally induced fluctuations. Experiments typically verify that with all EMI precautions, the observed switching rates or device electron temperature match the fridge temperature, indicating negligible excess heating.[52] Furthermore, laboratories often implement additional EMI countermeasures such as μ-metal shields for DC magnetic fields, spectrum analysis of environmental RF to eliminate specific offenders, and even RF absorbers on wiring to damp microwave resonances. By combining meticulous shielding, isolation and thermalization, electromagnetic disturbances and thermal noise can be suppressed to a "background" level, ensuring that stochastic switching in Josephson structures is driven by inherent quantum/thermal processes rather than external interference.

In this work, we present a fully integrated noise-reduction architecture built around a Bluefors LD-250 cryogen-free dilution refrigerator, designed to allow precision studies of Josephson junctions and related quantum electronic systems. This system has already been tested in our previous articles.[53–60]

The measurement system incorporates a multi-tier noise suppression framework, combining carefully shielded electronic instrumentation, low-temperature cryogenic RC filtering, and silver-epoxy-based microwave absorbers to mitigate high-frequency noise. A dedicated signal conditioning chain, incorporating room-temperature amplification and impedance-matched transmission lines, is employed to minimize external perturbations. Special attention is given to screening strategies for the sample holder, ensuring that spurious electromagnetic radiation and thermal leakage are effectively suppressed.

This paper is organized as follows: First, we provide a detailed description of the electronic measurement setup, including the configuration of amplifiers, switching matrices, and biasing circuits designed to suppress noise originating from room-temperature electronics. Next, we examine the low-temperature filtering mechanisms in detail, emphasizing their role in reducing spurious high-frequency components that could otherwise disturb delicate superconducting states. Finally, we demonstrate the effectiveness of this approach through a detailed characterization of switching current distributions in superconductor-insulator-superconductor (SIS) Josephson junctions, confirming that our system achieves signal purity at a level consistent with theoretical expectations for coherent quantum transport.

2. Electronic Setup

To ensure precise signal acquisition and noise suppression, we performed DC measurements using a Bluefors LD-250 dilution refrigerator, with an electromagnetically shielded copper sample holder. A four-point (Kelvin) contact method is implemented, utilizing separate twisted pairs (TPs) for current and voltage leads to minimize noise and exempt leads resistance during measurement.

The room-temperature equipment (amplifiers and their auxiliary circuits) is mounted in an electromagnetically shielded and grounded box directly connected to the cryostat via a standard, widely used 25-pin Fischer connector. This allows us to minimize the path of the low voltage non-amplified signal. The measured structure (voltage and current leads) is selected with low-noise commutation matrices (type 321, Ghielmetti). The swept excitation current source and voltage amplifier mounted in the box are connected to twisted pairs through matrices. So, it is possible to connect any of 24 lines in the cryostat to the measurement system. This allows to characterize up to 6 structures for each sample holder per one load. The amplified signals are sent to an analog-to-digital converter (ADC) using shielded cables. The bipolar power supply of the amplifier box (± 12 V) is filtered with 100 nF capacitors. Moreover, the swept signal input and amplified outputs are passed over Tusonix 4202-004LF pi-filters with insertion loss of 50 dB at 100 MHz and 70 dB at 1 GHz and even higher.

The schematic of an amplifier box is shown in Figure 2. The current bias to the sample is given by the external low-noise programmable voltage source over precision resistors. Different resistors can be alternatively connected to the circuit with the rotary switch in order to select the swept current range while holding the source range constant. Prior to resistors, the voltage signal V_0 is made symmetric ($+V_0/2$ and $-V_0/2$) to improve the resistivity to electromagnetic noise in twisted pairs. This is made with the symmetrization circuit based on two operational amplifiers (OP177 and LT1167). One of them is connected as a simple inverter without amplification, producing the negative part of a signal, and the other one is connected to the signal input and receives the inverted signal as a reference, making the positive part of a signal strictly negative to the positive part. Finally, this signal is sent to the cryostat via a twisted pair and passes to the sample through 4 K stage filters and a silver epoxy filter (**Figure** 1a). The voltage signal from the structure exits the cryostat via a twisted pair after being filtered at mK and 4 K stages. First, it is amplified with the first cascade instrumentation amplifier (AD8421) which has a very high input impedance of 30 GΩ, approaching the ideal voltmeter. Afterwards, it is amplified at the second cascade with operational amplifier working at closed loop feedback mode (LTC2057). The first cascade amplifier can provide a gain from 10 to 5000 (can be adjusted). The second cascade provides a gain from 1 to 10000 (also adjustable). The ground-connected gain-setting resistor of LTC2057 is selected as low as possible (100 Ω) to avoid the clock feed-through in the operational amplifier. Before the second cascade, the tunable active inverting band pass filter is installed (**Figure** 2d). The filter is based on the OP177 operational amplifier. Its cut-off frequency $f_c = \frac{1}{2\pi RC}$ with $R = 10$ KΩ can be varied from 15 Hz to 5.3 KHz by virtue of the variable capacitor. Every amplifier has the high input impedance and low output impedance, so there is a well impedance match and no signal drop between cascades.

The first cascade amplifier has the bandwidth in range from 2 to 10 MHz, depending on the selected gain. The second cascade amplifier has the bandwidth range from 150 Hz to 1.5 MHz. The low-pass RC filters installed in the cryostat (see later) can have the cut-off frequency of 1.592 KHz or 106 Hz, so one can select the amplification in order to perform *I*–*V* measurements at highest speed for any installed RC-filter.

The current bias signal is also amplified and passed to ADC in order to synchronously log an *I*–*V* curve. The symmetric bias signal is taken before the precision resistors, amplified with the AD8220 instrumentation amplifier and passed to an ADC. The active band-pass filter based on OP177 operational amplifier is also installed. To account for the voltage drop across the sample and correct the current signal accordingly, the voltage signal is measured using a second AD8421 amplifier connected in opposite polarity. This signal is then amplified by an INA132 instrumentation amplifier and provided as a reference to the AD8220 amplifier for the current signal. (Figure 2b).

One of the common problems of amplifier system is the floating zero (reference) that often drifts during the measurement procedure. The zero level of current and voltage output signals is controlled using the zero correction system. The precision reference voltage source (REF200) prepares the constant voltage which is adjusted with precision variable resistors (potentiometers), amplified with OP177 operational amplifiers and given to voltage (AD8421) and current (AD8220) amplifiers as a reference (Figure 2c).

All gains, including the first and second stages of voltage gain as well as the current gain, can be adjusted using variable resistors in the instrumentation amplifier control outputs and operational amplifier feedback circuits. This allows for the measurement of a wide range of samples with varying resistances and critical currents while maximizing voltage resolution and utiliz-

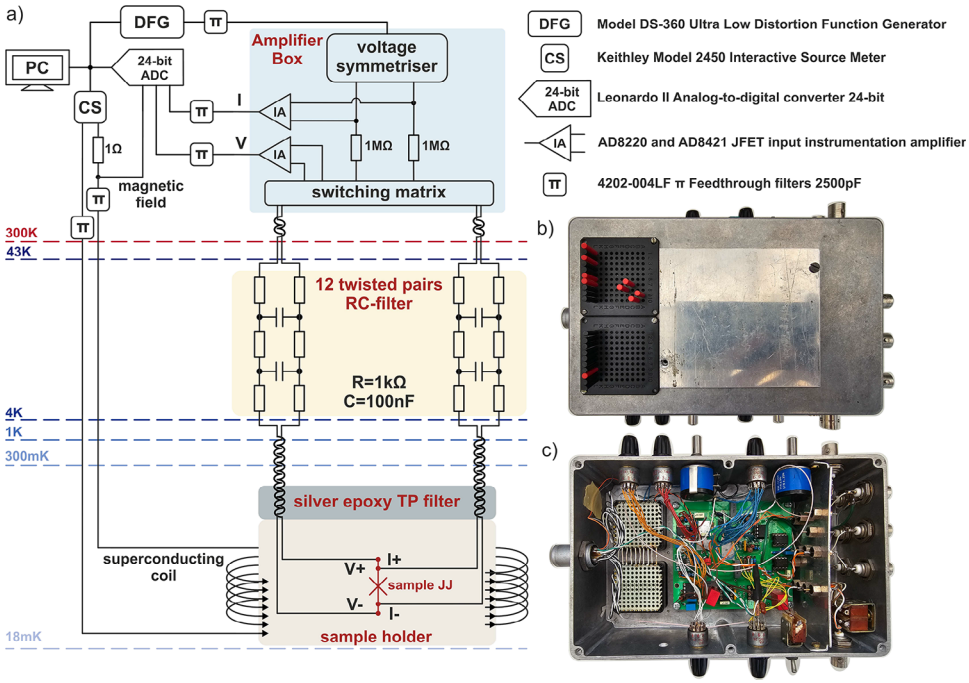

Figure 1. Room temperature measurement equipment. a) Simplified block diagram of a measurement system. All connections from the amplifier box are shown. b) Amplifier box overview. The switching matrices (at the bottom part of the box) and knobs for amplification and offset adjustment (on the left and right walls) are visible. c) Amplifier box with opened lid, a printed circuit board with amplification circuits is visible. The Fischer 25-pin male connector is located on the box's left wall. It is connected directly to the female connector on the top of the dilution refrigerator. A partition with pi-filters for input and output signals is located near the right wall.

ing the full range of the ADC input. Adjustable knobs are shown in Figure 2 as red rectangles with labels.

A 24-bit ADC system synchronously digitizes voltage, current, and magnetic field signals at a sampling rate of 102.4 kHz, ensuring high-resolution data acquisition. Over an extended measurement period, stable and reproducible behavior in Josephson structures is observed, confirming the reliability of the system. Noise tests on an Al/AlO_x/Al Josephson junction (normal resistance is 5 kΩ with a theoretical critical current 50 nA) results a measured switching current of 30 nA, verifying that current noise amplitude remains below 10 nA, well within the requirements for sub-μA critical current measurements.

3. RC Filters

To achieve optimal noise suppression, our setup employs a series of cryogenic low-pass RC filters positioned at different temperature stages of the dilution refrigerator. These filters are crucial in mitigating Johnson–Nyquist noise, reducing unwanted thermal excitations, and filtering out electromagnetic interference across a broad frequency range. Low temperatures T_C of a measured sample require higher attenuations of unwanted frequencies from higher temperatures T:[61]

$$A(f) = \frac{e^{\frac{hf}{kT}} - 1}{e^{\frac{hf}{kT_C}} - 1}, \tag{1}$$

so in order to protect the millikelvin-temperatured sample from high-frequency noise from high temperatures, the filters must be installed at different stages of a cryostat. The first stage is typically 4 K.[61]

An **RC Low-Pass Filter** allows low-frequency signals to pass while attenuating higher frequencies. It consists of a series resistor (R) and a shunt capacitor (C) from the output to ground. A constant DC input to the resistor results in a constant DC voltage across the capacitor. A change in the DC input voltage will result in the capacitor gradually charging/discharging to match the input voltage after a time delay. However, a high-frequency fluctuation in the input will not give the capacitor enough time to react - it will undergo a smaller change in voltage, thereby maintaining an output signal with damped fluctuation. To block the whole spectrum of unwanted frequencies, the R-C circuit is repeated (**Figure 3c**). The filter cutoff frequency can be expressed as:

$$f_c = \frac{1}{2\pi RC} \tag{2}$$

The transfer function of the RC filter is given by:

$$H(f) = \frac{1}{1 + j2\pi fRC} \tag{3}$$

where j is the imaginary unit. The magnitude of the gain is:

$$|H(f)| = \frac{1}{\sqrt{1 + (2\pi fRC)^2}} \tag{4}$$

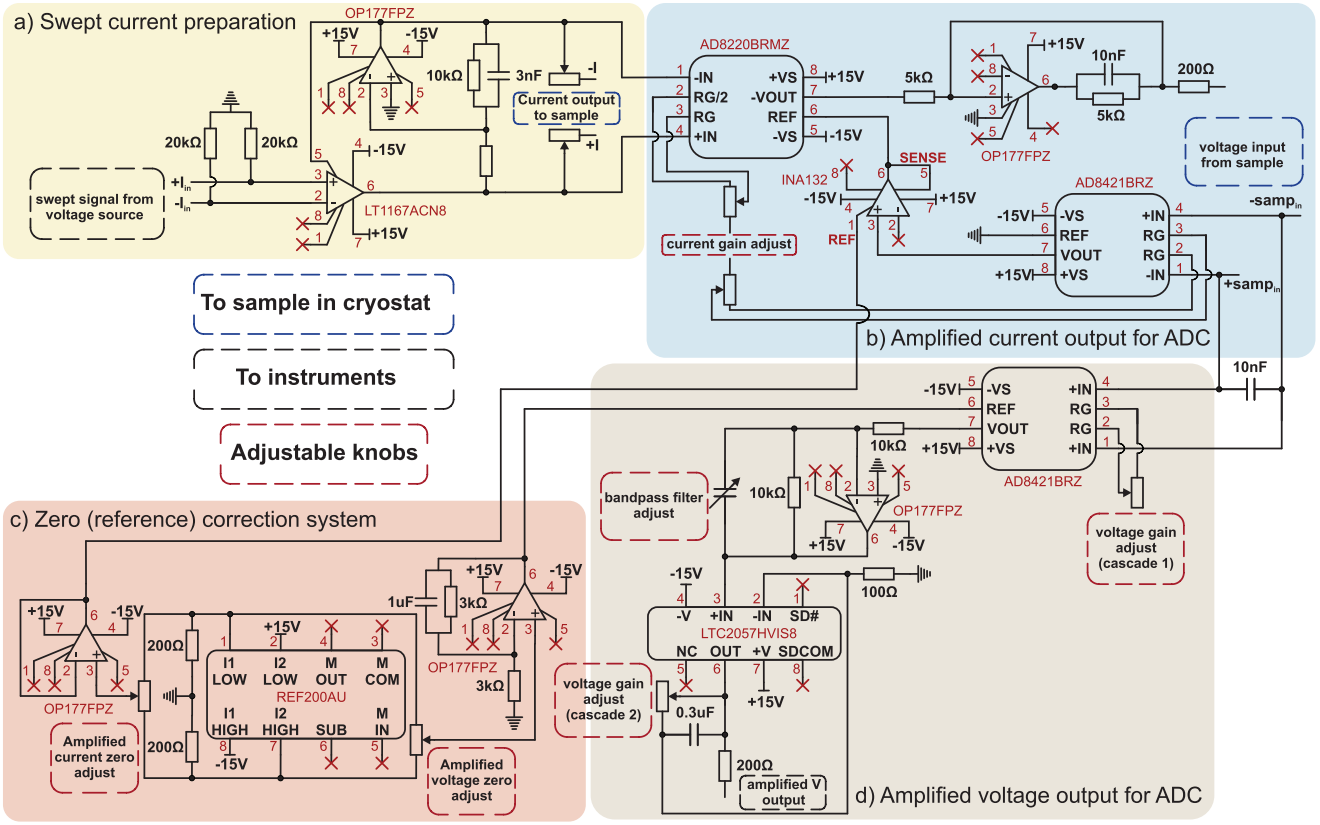

Figure 2. Room-temperature amplifier box schematic. Some logical parts are shown by dashed rectangles of different color: swept current preparation, making an amplified output signal for sample current and voltage for ADC board, and zero (offset) adjustment. Connections from voltage source and ADC board are marked with magenta rectangles. Connections to a sample in a cryostat are marked with blue rectangles. User-adjustable knobs (gain selection, offset tuning) are marked with red rectangles.

The gain in decibels (dB) is given by:

$$G(f) = 20\log_{10}|H(f)| \tag{5}$$

For samples of different resistance and critical current, different values of filter resistance are used, allowing to avoid too large voltages on measurement leads. Moreover, the resulting cutoff frequency limits the speed of the I-V curve measurement and must be chosen according to the sweep speed. For samples with low critical current (for example, sub-micron SIS junctions) the filters with $R = 15\text{k}\Omega$ and $C = 100\text{nF}$ are used, thus the cutoff frequency here is $f_c = 106$ Hz. For samples with high critical currents, where some milliamperes must be passed over the measurement system, the optimal values are $R = 1\text{k}\Omega$ and $C = 100\text{nF}$, which yields the cutoff frequency $f_c = 1.592$ KHz.

The simulation result for an RC-filter with $R = 1\text{k}\Omega$ and $C = 100\text{nF}$ is shown in Figure 3d.

Each RC filter assembly consists of high-precision surface-mounted resistors and capacitors chosen for cryogenic performance. The resistors are made of thin-film metal-oxide material which minimizes resistance drift at low temperatures, while the capacitors utilize multilayer ceramic dielectric materials designed for stable capacitance at 4 K temperature stage (NP0 ceramics). All components were carefully tested in the whole range of cryogenic temperatures, and the absence of strong resistance/capacitance drift was confirmed. These filters are carefully thermally anchored at each temperature stage to ensure effective cooling and prevent any parasitic heating from interfering with the superconducting junctions. Resistors and capacitors are located on a PCB which contains top and internal copper layers to improve the cooling of the PCB. The PCB is mounted in the copper housing and thermally anchored to it (Figure 3b). The housing is closed to protect the filter circuit from non-equilibrium photons from the 4 K cryostat stage. The filter assembly is equipped with standard Micro-D-Sub connectors compatible with standard Bluefors DC lines (Figure 3a).

Experimental tests confirm that these filters reduce high-frequency signal noise by more than 90 dB, enabling precise current–voltage measurements without external contamination.

4. Sample Holder and Silver-Epoxy Filters

The sample holder is designed to provide optimal electromagnetic shielding and thermalization. On the outside of the holder, it is possible to install two concentric shields 50 and 60 mm in diameter made of mu-metal (**Figure** 4a red and blue parts). Instead of mu-metal shields, it is also possible to install a brass shield with a solenoid on the surface for measuring samples with a magnetic field. The Cu-made holder body consists of two parts connected by 4 bolts through supports. This design makes it pos-

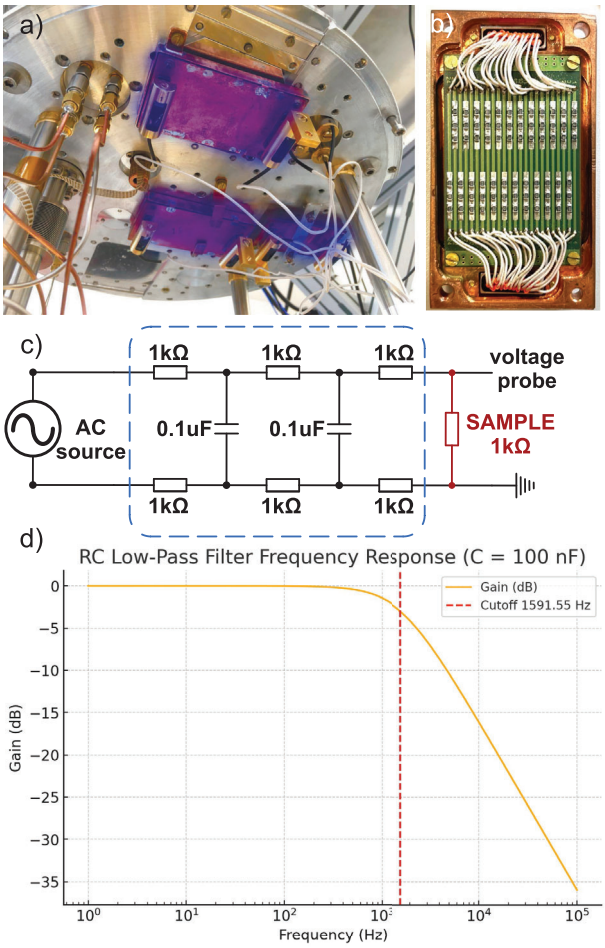

Figure 3. Low-temperature RC filters for 4 K cryostat plate. a) Photo of 4 K flange of Bluefors LD series dilution refrigerator with installed RC filters (false-colored with violet).) Filter assembly without a lid. A PCB with installed resistors and connection wires to Micro D-Sub connectors are visible. c) Simulation of RC filter transition at different frequencies; the blue dashed rectangle shows the filter itself. d) simulation results. A gain decrement after the cutoff frequency is visible.

sible to install caps for each of the shields. The caps have holes for the output cables.

A carrier with sample is located in the area near the bottom of the shields (Figure 4a orange part). It has 24 DC contacts and 6 RF lines, which are located in the intermediate layer of the pcb for wire bonding. The sample carrier has 24 additional DC connectors on both sides to ground the sample during wire bonding and installation in the cryostat (Figure 4b black connector). To shield the sample from IR radiation, the sample carrier is closed from above with a copper lid.

A specially designed Ag-epoxy cryogenic powder filter is placed in the holder case (Figure 4a yellow part). It provides thermalization of DC lines and high-frequency attenuation. The filter consists of 12 twisted pairs of 0.1 mm diameter and 1.5 m long Cu-wire covered in polyurethane lacquer and wound bifilarly on a copper coil (**Figure** 5a). During the winding process, each twisted pair is coated with a layer of conductive silver-epoxy composite(Figure 5b). In our case we use RS PRO Silver Conductive Lacquer that dries up quickly. We also use 25-pin J30J Cinch to connect the sample holder to the DC lines of the cryostat (Figure 4c).

The copper wire and the conductive silver composite are a distributed RC filter with high resistance and capacitance and low inductance. Due to the skin effect, a high-frequency parasitic signal propagates near the surface of the wire through a cross-section with an area of $\pi\delta D^2$, where $\delta = 1/\sqrt{\sigma_{cu}\mu_{cu}\pi f}$ is skin depth. The effective resistance of the transmission line increases with increasing frequency and the filter attenuates the parasitic signal. The attenuation also increases proportionally with the length of the wires. A rough estimate of the filter characteristics gives R = 3.2 Ohm, C = 0.98 nF, L = 76 nH. In Figure 5c, the measurements of the transmission S-parameter of the filter are presented. Measurements were performed with the Rohde&Schwarz ZNB vector network analyzer at the input signal power of –20 dBm with the sensing bandwidth of 100 Hz. The frequency sweep was of 100001 points from 9 KHz to 10 GHz. The attenuation at high frequencies is up to –100 dB ensuring that no external RF interference affects the measurements.

5. Verification Part

We characterize our system by measuring the switching current distribution of 200x200 nm^2 SIS Josephson junctions (**Figure** 6a) made by the Al-AlOx-Al shadow evaporation technology.[62–64] First, a 100 nm thick Al layer was deposited onto the high-resistive Si substrate using Plassys MEB550s e-beam evaporation system. Next, the lines and bonding pads were created using the direct-laser lithography system (μMLA, Heidelberg Instruments) and etched with dry etching technique (1000 Volts, 50 mA, for 10 min, using KDC-40 ion gun KauffmanSource, and argon). For shadow evaporation, two layers of electron resist: methyl methacrylate (500 nm) and polymethyl methacrylate (100 nm) were applied. Then, a Josephson junction geometry was defined with e-beam lithography (JEOL 7001f). First electrode was evaporated using the e-beam system at angle $\alpha_1 = -20deg$, then it was oxidized at 20 mBar during 10 min, and, finally, the second electrode was evaporated at angle $\alpha_2 = +20deg$. Finally, the resist was removed with the lift-off process emmerced in acetone for 3 h, rinse using siringe and finaly remove resist residues in an ultrasonic bath for 1 min.

Figure 6a shows a scanning electron microscope (SEM) image of our Josephson junction and its schematic 3D representation. The insulating layer is highlighted in red. Figure 6b illustrates the I–V characteristics measured by both the analog and digital (commercially available) systems. The Digital system was based on Keithley 6220 current source and Keithley 2182a nanovoltmeter. The current source range was selected as a minimal range to cover required swept currents. The signal from the current source was supplied via the triaxial cable (output high via the central conductor and output low via the inner shield). The nanovoltmeter was set up to Autorange, with the measurement time of 5 power-line AC voltage cycles. The voltade signal was fed to the nanovoltmeter using the shielded twisted pair. The critical currents differ by nearly a factor of two. The gray dotted line represents the critical current calculated using the Ambegaokar–Baratoff formula.[65] The observed switching cur-

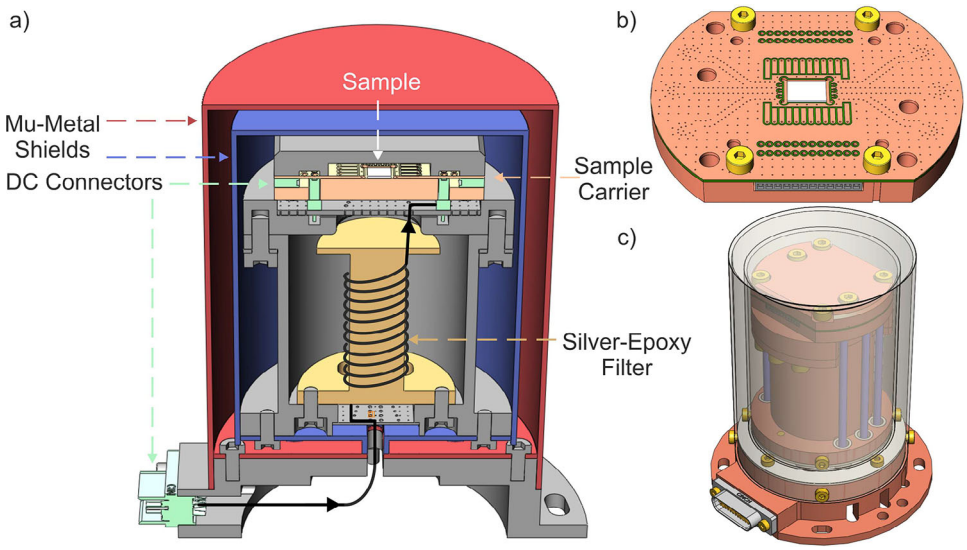

Figure 4. Sample holder. a) Schematic representation of the cross-section of the sample holder. b) Sample carrier part. A white rectangle schematically indicates a chip with a sample. c) Full setup.

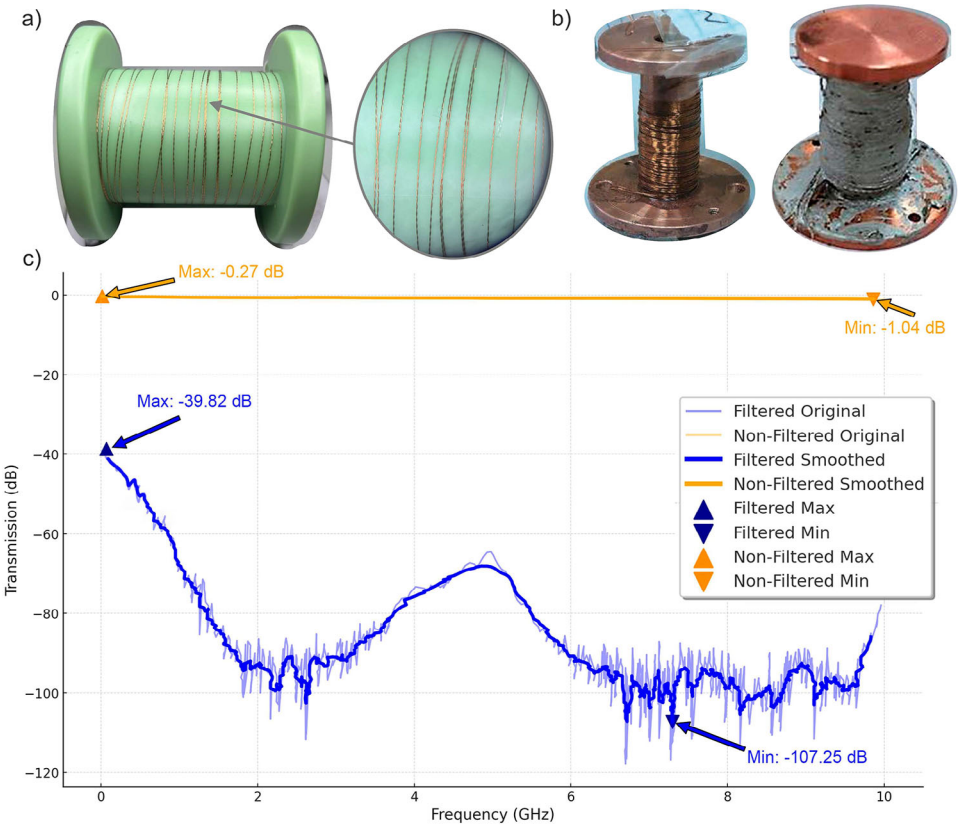

Figure 5. Low-temperature distributed powder RC-filter for high frequencies: fabrication and testing. a) Preparing of twisted pairs from varnished 0.1 mm wires. b) Winding of twisted pairs onto the copper base and fixing them with epoxy containing silver powder. c) Test of filter using the vector network analyzer. Top: measuring of cable transmission S-parameter for reference. Bottom: measuring the transmission S-parameter of a filter.

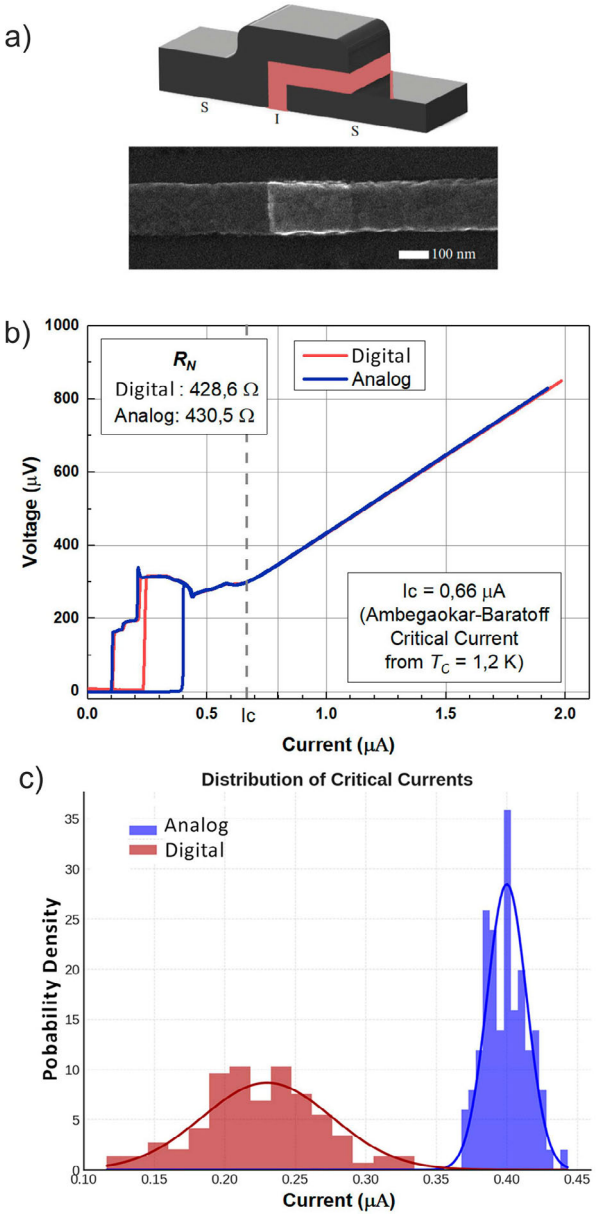

Figure 6. Test of measurement system. a) Test structure for testing: Aluminium SIS junctions with aluminum oxide barrier. Top: junction 3D model, bottom: SEM image of a junction. b) Example of *I–V* curves measured with our proposed measurement system (blue curve) and Digital system "precision current source + nanovoltmeter" pair. The switching current for our system is 400 nA, which is almost twice more than the switching current for the Digital system (220 nA). The theoretically predicted critical current is 0.66 μA. c) Distribution of switching currents measured by two measurement systems and their Gaussian fits.

rent aligns closely with the critical current expected using the Ambegaokar–Baratoff theory:

$$I_C = \frac{\pi\Delta}{2R_N} \tag{6}$$

where Δ is the superconducting gap and R_N is the normal-state resistance of the junction. The superconducting gap Δ can be estimated from the superconducting transition temperature T_C using the Bardeen-Cooper-Schrieffer[66] theory:

$$\Delta = 1.76 k_B T_C \tag{7}$$

where k_B is the Boltzmann constant. We can compare the experimentally measured critical currents with theoretical expectations and confirm that the noise level in the measurement system is low enough.

To measure the switching current distribution, the method of double threshold was used. The current was swept upwards from zero and the voltage was tracked continuously. When the voltage overcomes the first threshold $\epsilon_1 = 4$ μV, the threshold changes to $\epsilon_2 = 7$ μV. When the voltage overcomes ϵ_2, the corresponding current value is treated as the observed critical current. This method allows to obtain the critical current distribution quickly, without measuring the whole *I–V* curve, and avoid wrong measurement of a critical current due to near-zero voltage noise. The threshold values can be adjusted depending on the noise level and the resistance of the measured sample.

The incorporation of multi-stage filtering significantly improves signal fidelity. By comparing measurements with and without additional cryogenic attenuation, we observe a 60 times reduction in signal broadening, highlighting the effectiveness of our approach. Furthermore, the optimized shielding and ground isolation prevent thermal and electromagnetic noise from corrupting experimental data, establishing our system as a highly reliable platform for quantum-coherent transport studies.

We experimentally measured the distribution of critical currents in two different systems: the **Analog System** (presented in this manuscript) and the **Digital System** widely used to measure *I–V* curves of Josephson structures. We conducted measurements 100 times for each system. The resulting distributions are shown in Figures 6 and 7.

After obtaining the experimental data, we applied a Gaussian fit to analyze the statistical properties and determine the spread in each case. The Gaussian function used for fitting is given by:

$$P(I) = \frac{1}{\sigma\sqrt{2\pi}} \exp\left(-\frac{(I-\mu)^2}{2\sigma^2}\right), \tag{8}$$

where:

- $P(I)$ is the probability density function of the critical current I,
- μ is the mean critical current,
- σ is the standard deviation, representing the spread of the distribution.

The **Table 1** below summarizes the key differences between the analog and digital measurement systems:

Table 1. Comparison of the analog and digital measurement systems.

Parameter	Analog System	Digital System
Ic (μ)	0.4 μA	0.23 μA
Spread (σ)	0.014 μA (3.5)	0.046 μA (20)
Signal-to-Noise Ratio	High	Low

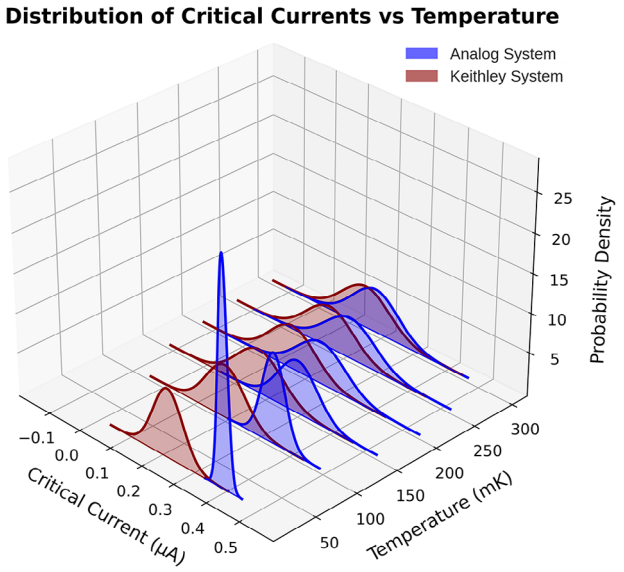

Figure 7. Probability density of the critical current distribution change with temperature The switching current change $P(I - <I>)$ is analyzed over the temperature range of $T = 25$mK to $T = 300$mK. The current distribution is plotted both for the analog (blue) and the commercially available digital (red) measurement systems. At higher temperatures the distribution of both systems overlap, while upon cooling, differences gradually emerge, leading to a complete separation at 25mK.

The results indicate that the Analog System provides a significantly narrower and well-defined peak in the critical current distribution, indicating minimal fluctuations and a higher degree of measurement precision. Conversely, the digital system exhibits a broader distribution, indicating a higher noise level and variability in the critical current measurements.

The critical current distributions for both systems were measured at different temperatures, see **Figure** 7. At the base temperature of the dilution refrigerator, there is a vast difference in distributions, as shown before. The increase in temperature makes the distributions wider, and at a temperature of ∼ 300 mK, distributions become almost equal, and the advantage of our measurement system disappears. This allows us to conclude that while using our system, the low noise level yields a decrease in the electron temperature of a sample. The electron temperature is higher in commercially available measurement systems due to a higher noise level. When a cryostat is heated to ∼ 200 mK, the difference disappears because the electron temperature in both systems rises to an equal level.

6. Conclusion

Our findings demonstrate that Josephson switching current measurements can be conducted with high precision by integrating advanced filtering, shielding, and signal conditioning techniques. The combination of low-noise amplifiers, multi-stage cryogenic filtering, and optimized electromagnetic shielding ensures that noise sources are effectively suppressed, allowing the intrinsic properties of superconducting structures to be probed with greater accuracy than commercial systems. This methodology provides a foundation for quantum superconducting electronics and topological superconductivity experiments.

Acknowledgements

The work of I.A.N and V.L.G. was supported by Rosatom in the framework of the Roadmap for Quantum computing (Contract No. 868-1.3-15/15-2021 dated October 5). The work of D.S.Ya was supported by ANR Quantum (ANR 725-23-42) and by Airbus through a Co-fund fellowship. The characterization of Josephson junctions was supported by a Grant from the Ministry of Science and Higher Education No. 075-15-2024-632. The work of I.A.N. in the field of low-temperature experiment was supported by the Russian science foundation grant № 25-22-20055 https://rscf.ru/project/25-22-20055/

Conflict of Interest

The authors declare no conflict of interest.

Author Contributions

D.S.Ya. and V.L.G. suggested the idea of the experiment; D.S.Ya., V.S.S, and V.V.R. conceived the project and supervised the experiments; V.L.G., V.S.S, and S.V.E. designed and fabricated the room-temperature amplifier and RC-filters. G.I.G. designed, fabricated and tested the sample holder. D.S.Ya., I.A.N., J.S., and S.M.R. performed the low-temperature experiments. G.I.G. made visualization. D.S.Ya. and I.A.N. wrote the manuscript with input from all authors. All authors discussed the results and their implications equally.

Data Availability Statement

The data that support the findings of this study are available from the corresponding author upon reasonable request.

Keywords

amplifier, DC measurements, Josephson junction, low noise signal, RC-filters

Received: March 17, 2025
Revised: April 26, 2025
Published online:

[1] Y. Makhlin, G. Schön, A. Shnirman, *Rev. Mod. Phys.* **2001**, *73*, 357.
[2] D. Vion, P. Orfila, P. Joyez, D. Esteve, M. Devoret, *J. Appl. Phys.* **1995**, *77*, 2519.
[3] H. Courtois, O. Buisson, J. Chaussy, B. Pannetier, *Rev. Sci. Instrum.* **1995**, *66*, 3465.
[4] H. le Sueur, P. Joyez, *Rev. Sci. Instrum.* **2006**, *77*, 11.
[5] A. Zorin, *Rev. Sci. Instrum.* **1995**, *66*, 4296.
[6] D. Glattli, P. Jacques, A. Kumar, P. Pari, L. Saminadayar, *J. Appl. Phys.* **1997**, *81*, 7350.
[7] E. Mykkänen, J. Lehtinen, A. Kemppinen, C. Krause, D. Drung, J. Nissilä, A. Manninen, *Rev. Sci. Instrum.* **2016**, *87*, 10.
[8] F. Mueller, R. N. Schouten, M. Brauns, T. Gang, W. H. Lim, N. S. Lai, A. S. Dzurak, W. G. van der Wiel, F. A. Zwanenburg, *Rev. Sci. Instrum.* **2013**, *84*, 4.
[9] L. Longobardi, D. A. Bennett, V. Patel, W. Chen, J. E. Lukens, *Rev. Sci. Instrum.* **2013**, *84*, 1.
[10] D. Slichter, O. Naaman, I. Siddiqi, *Appl. Phys. Lett.* **2009**, *94*, 19.
[11] D. Santavicca, D. Prober, *Meas. Sci. Technol.* **2008**, *19*, 087001.

[12] J. M. Martinis, M. H. Devoret, J. Clarke, *Phys. Rev. B* **1987**, *35*, 4682.
[13] A. Fukushima, A. Sato, A. Iwasa, Y. Nakamura, T. Komatsuzaki, Y. Sakamoto, *IEEE Trans. Instrum. Meas.* **1997**, *46*, 289.
[14] F. Milliken, J. Rozen, G. Keefe, R. Koch, *Rev. Sci. Instrum.* **2007**, *78*, 2.
[15] A. Lukashenko, A. Ustinov, *Rev. Sci. Instrum.* **2008**, *79*, 1.
[16] C. P. Scheller, S. Heizmann, K. Bedner, D. Giss, M. Meschke, D. M. Zumbühl, J. D. Zimmerman, A. C. Gossard, *Appl. Phys. Lett.* **2014**, *104*, 21.
[17] A. I. Ivanov, V. I. Polozov, V. V. Echeistov, A. A. Samoylov, E. I. Malevannaya, A. R. Matanin, N. S. Smirnov, I. A. Rodionov, *Appl. Phys. Lett.* **2023**, *123*, 20.
[18] W.-S. Lu, K. Kalashnikov, P. Kamenov, T. J. DiNapoli, M. E. Gershenson, *Electronics* **2023**, *12*, 416.
[19] I. Jin, A. Amar, F. Wellstood, *Appl. Phys. Lett.* **1997**, *70*, 2186.
[20] M. V. Moghaddam, C. Chang, I. Nsanzineza, A. Vadiraj, C. Wilson, *Appl. Phys. Lett.* **2019**, *115*, 21.
[21] L. Spietz, J. Teufel, R. Schoelkopf, *arXiv preprint cond-mat/0601316* **2006**.
[22] H. Bluhm, K. A. Moler, *Rev. Sci. Instrum.* **2008**, *79*, 1.
[23] A. Paquette, J. Griesmar, G. Lavoie, R. Albert, F. Blanchet, A. Grimm, U. Martel, M. Hofheinz, *Appl. Phys. Lett.* **2022**, *121*, 12.
[24] W. Pan, J.-S. Xia, V. Shvarts, D. Adams, H. Stormer, D. Tsui, L. Pfeiffer, K. Baldwin, K. West, *Phys. Rev. Lett.* **1999**, *83*, 3530.
[25] K. Kang, H. Berger, K. Watanabe, T. Taniguchi, L. Forró, J. Shan, K. F. Mak, *Nano Lett.* **2022**, *22*, 5510.
[26] M. Sahu, *Switching current distributions of superconducting nanowires: Evidence of quantum phase slip events*, University of Illinois at Urbana-Champaign, **2009**.
[27] K. Bladh, D. Gunnarsson, E. Hürfeld, S. Devi, C. Kristoffersson, B. Smålander, S. Pehrson, T. Claeson, P. Delsing, M. Taslakov, *Rev. Sci. Instrum.* **2003**, *74*, 1323.
[28] I. N. Moskalenko, I. A. Simakov, N. N. Abramov, A. A. Grigorev, D. O. Moskalev, A. A. Pishchimova, N. S. Smirnov, E. V. Zikiy, I. A. Rodionov, I. S. Besedin, *npj Quantum Inf.* **2022**, *8*, 130.
[29] X. Wei, J. Jiang, W. Xu, T. Guo, K. Zhang, Z. Li, T. Zhou, Y. Sheng, C. Cao, G. Sun, P. Wu, *Appl. Phys. Lett.* **2023**, *123*, 15.
[30] A. Wallraff, A. Lukashenko, C. Coqui, A. Kemp, T. Duty, A. Ustinov, *Rev. Sci. Instrum.* **2003**, *74*, 3740.
[31] H. De Oliveira, P. Marmillod, C. Theiler, R. Chavan, O. Février, B. Labit, P. Lavanchy, B. Marlétaz, R. Pitts, *Rev. Sci. Instrum.* **2019**, *90*, 8.
[32] M. Onyszczak, A. J. Uzan-Narovlansky, Y. Tang, P. Wang, Y. Jia, G. Yu, T. Song, R. Singha, J. F. Khoury, L. M. Schoop, S. Wu, *Rev. Sci. Instrum.* **2023**, *94*, 10.
[33] S. Bolduc Beaudoin, E. Pinsolle, B. Reulet, *Physical Review Research* **2024**, *6*, 043238.
[34] R. H. Koch, D. Van Harlingen, J. Clarke, *Phys. Rev. Lett.* **1980**, *45*, 2132.
[35] Y. A. Pashkin, O. Astafiev, T. Yamamoto, Y. Nakamura, J. Tsai, *Quantum Inf. Process.* **2009**, *8*, 55.
[36] N. Ohmura, S. Ogino, Y. Okano, in *2014 International Symposium on Electromagnetic Compatibility, Tokyo*, IEEE, **2014**, pp. 765–768.
[37] H.-S. Yeo, S. Woo, J. Kim, Y. Kim, B. Choi, G. Choi, J. Choi, S. K. Lee, W. Song, Y. Chong, *IEEE Trans. Appl. Supercond.* **2023**, *33*, 1.
[38] D. Vion, A. Aassime, A. Cottet, P. Joyez, H. Pothier, C. Urbina, D. Esteve, M. H. Devoret, *Science* **2002**, *296*, 886.
[39] J. Clarke, A. I. Braginski, *The SQUID handbook: Applications of SQUIDs and SQUID systems*, John Wiley & Sons, **2006**.
[40] S. Zhu, S. Peng, Z. Qiang, C. Ye, M. Zhu, *Carbon* **2022**, *193*, 258.
[41] Y. V. Nazarov, *Quantum noise in mesoscopic physics*, vol. *97*, Springer Science & Business Media, **2012**.
[42] J. M. Martinis, M. H. Devoret, J. Clarke, *Phys. Rev. Lett.* **1985**, *55*, 1543.
[43] A. Osman, J. Fernández-Pendás, C. Warren, S. Kosen, M. Scigliuzzo, A. Frisk Kockum, G. Tancredi, A. Fadavi Roudsari, J. Bylander, *Phys. Rev. Res.* **2023**, *5*, 043001.
[44] S. Kosen, H.-X. Li, M. Rommel, R. Rehammar, M. Caputo, L. Grönberg, J. Fernández-Pendás, A. F. Kockum, J. Biznárová, L. Chen, C. Križan, A. Nylander, A. Osman, A. F. Roudsari, D. Shiri, G. Tancredi, J. Govenius, J. Bylander, *PRX Quantum* **2024**, *5*, 030350.
[45] R. Barends, J. Kelly, A. Megrant, D. Sank, E. Jeffrey, Y. Chen, Y. Yin, B. Chiaro, J. Mutus, C. Neill, P. O'Malley, P. Roushan, J. Wenner, T. C. White, A. N. Cleland, J. M. Martinis, *Phys. Rev. Lett.* **2013**, *111*, 080502.
[46] A. Somoroff, Q. Ficheux, R. A. Mencia, H. Xiong, R. Kuzmin, V. E. Manucharyan, *Phys. Rev. Lett.* **2023**, *130*, 267001.
[47] A. D. Córcoles, J. M. Chow, J. M. Gambetta, C. Rigetti, J. R. Rozen, G. A. Keefe, M. Beth Rothwell, M. B. Ketchen, M. Steffen, *Appl. Phys. Lett.* **2011**, *99*, 18.
[48] O. Kieler, B. Karlsen, P. A. Ohlckers, E. Bardalen, M. N. Akram, R. Behr, J. Ireland, J. Williams, H. Malmbekk, L. Palafox, R. Wendisch, *IEEE Trans. Appl. Supercond.* **2019**, *29*, 1.
[49] J. A. Schreier, A. A. Houck, J. Koch, D. I. Schuster, B. R. Johnson, J. M. Chow, J. M. Gambetta, J. Majer, L. Frunzio, M. H. Devoret, S. M. Girvin, R. J. Schoelkopf, *Phys. Rev. B: Condens. Matter Mater. Phys.* **2008**, *77*, 180502.
[50] Y.-C. Chang, B. Karimi, J. Senior, A. Ronzani, J. T. Peltonen, H.-S. Goan, C.-D. Chen, J. P. Pekola, *Appl. Phys. Lett.* **2019**, *115*, 2.
[51] A. Krasnok, P. Dhakal, A. Fedorov, P. Frigola, M. Kelly, S. Kutsaev, *Appl. Phys. Rev.* **2024**, *11*, 1.
[52] S. Simbierowicz, M. Borrelli, V. Monarkha, V. Nuutinen, R. E. Lake, *PRX Quantum* **2024**, *5*, 030302.
[53] V. S. Stolyarov, D. S. Yakovlev, S. N. Kozlov, O. V. Skryabina, D. S. Lvov, A. I. Gumarov, O. V. Emelyanova, P. S. Dzhumaev, I. V. Shchetinin, R. A. Hovhannisyan, S. V. Egorov, A. M. Kokotin, W. V. Pogosov, V. V. Ryazanov, M. Y. Kupriyanov, A. A. Golubov, D. Roditchev, *Commun. Mater.* **2020**, *1*, 38.
[54] V. S. Stolyarov, D. Roditchev, V. L. Gurtovoi, S. N. Kozlov, D. S. Yakovlev, O. V. Skryabina, V. M. Vinokur, A. A. Golubov, *Adv. Quantum Technol.* **2022**, *5*, 2100124.
[55] D. S. Yakovlev, I. A. Nazhestkin, N. G. Ismailov, S. V. Egorov, V. N. Antonov, V. L. Gurtovoi, *Symmetry* **2023**, *15*, 550.
[56] A. F. Shevchun, G. K. Strukova, I. M. Shmyt'ko, G. V. Strukov, S. A. Vitkalov, D. S. Yakovlev, I. A. Nazhestkin, D. V. Shovkun, *Symmetry* **2022**, *14*, 2142.
[57] D. S. Yakovlev, A. V. Frolov, I. A. Nazhestkin, A. G. Temiryazev, A. P. Orlov, J. Shvartzberg, S. E. Dizhur, V. L. Gurtovoi, R. Hovhannisyan, V. S. Stolyarov, *Adv. Phys. Res.* **2024**, *3*, 2400108.
[58] I. A. Nazhestkin, S. V. Bakurskiy, A. A. Neilo, I. E. Tarasova, N. G. Ismailov, V. L. Gurtovoi, S. V. Egorov, S. A. Lisitsyn, V. S. Stolyarov, V. N. Antonov, V. V. Ryazanov, M. Y. Kupriyanov, I. I. Soloviev, N. V. Klenov, D. S. Yakovlev, *Adv. Eng. Mater.* **2025**, 2402385.
[59] A. Shishkin, O. Skryabina, V. Gurtovoi, S. Dizhur, M. Faley, A. Golubov, V. Stolyarov, *Supercond. Sci. Technol.* **2020**, *33*, 065005.
[60] V. Lubsanov, V. Gurtovoi, A. Semenov, E. Glushkov, V. Antonov, O. Astafiev, *Supercond. Sci. Technol.* **2022**, *35*, 105013.
[61] M. Thalmann, H.-F. Pernau, C. Strunk, E. Scheer, T. Pietsch, *Rev. Seeci. Instrum.* **2017**, *88*, 11.
[62] D. O. Moskalev, E. V. Zikiy, A. A. Pishchimova, D. A. Ezenkova, N. S. Smirnov, A. I. Ivanov, N. D. Korshakov, I. A. Rodionov, *Sci. Rep.* **2023**, *13*, 4174.
[63] A. A. Pishchimova, N. S. Smirnov, D. A. Ezenkova, E. A. Krivko, E. V. Zikiy, D. O. Moskalev, A. I. Ivanov, N. D. Korshakov, I. A. Rodionov, *Sci. Rep.* **2023**, *13*, 6772.
[64] N. D. Korshakov, D. O. Moskalev, A. A. Soloveva, D. A. Moskaleva, E. S. Lotkov, A. R. Ibragimov, M. V. Androschuk, I. A. Ryzhikov, Y. V. Panfilov, I. A. Rodionov, *Sci. Rep.* **2024**, *14*, 26066.
[65] V. Ambegaokar, A. Baratoff, *Phys. Rev. Lett.* **1963**, *10*, 486.
[66] J. Bardeen, L. N. Cooper, J. R. Schrieffer, *Phys. Rev.* **1957**, *108*, 1175.